Flow (2025), **5** E43
doi:10.1017/flo.2025.10036

FLOW CAMBRIDGE UNIVERSITY PRESS

RESEARCH ARTICLE

Direct numerical simulations of turbulent flows through porous media using a spectral difference method solver

Adrian Rusnak, Francois Chedevergne and Rémi Roncen

DMPE, ONERA, Université de Toulouse, 31000, Toulouse, France
Corresponding author: Adrian Rusnak; Email: adrian.rusnak@onera.fr

Received: 12 June 2025; **Revised:** 15 September 2025; **Accepted:** 3 November 2025

Keywords: turbulence simulation; porous media; spectral difference method; immersed boundary conditions; pressure gradient scaling

Abstract

This study presents a high-fidelity direct numerical simulation (DNS) framework tailored for investigating turbulent flows through complex porous structures. It employs a compressible Navier–Stokes solver based on the spectral difference (SD) method, with immersed boundary conditions (IBCs) implemented via the Brinkman penalisation technique and integrated using a Strang splitting approach. A pressure gradient scaling (PGS) strategy is incorporated to improve computational efficiency. To provide realistic inflow conditions, synthetic turbulence is injected at the inlet using a random Fourier modes method. The methodology is validated in several stages. First, the IBC approach is tested against results from a body-fitted mesh, showing strong agreement in the mean velocity field. Next, the effectiveness of the PGS technique is demonstrated by comparing scaled and unscaled simulations, both of which yield consistent velocity fields and spectral content. Finally, the full DNS-SD framework is benchmarked against finite volume method results from the literature, successfully reproducing key turbulence characteristics, including two-point correlations. The validated solver is ultimately applied to simulate turbulent flow through a complex porous geometry. The results illustrate the robustness of the approach and highlight its potential for advancing the understanding of turbulence in porous materials.

Impact statement

Porous media play a vital role in various engineering applications, including combustion systems, heat exchangers, aero-acoustics and filtration. However, interactions between their complex geometries and turbulent flows pose significant challenges for numerical simulation, especially in mesh generation and time-step restrictions. This work introduces a high-fidelity simulation framework that overcomes these challenges by enabling accurate low-Mach-number simulations of turbulent flows through porous structures, while significantly reducing meshing complexity and computational cost. Additionally, the introduction of a synthetic turbulence injection at the inlet provides realistic inflow conditions, enhancing the practical relevance of simulations. These capabilities are particularly relevant for developing ultra-low emission combustion technologies, where turbulence–porous medium interactions critically influence flame stability, efficiency and pollutant formation.

1. Introduction

Porous media play a crucial role in various industries, including energy, chemical processing and environmental engineering, due to their ability to influence the flow dynamics and for example promote heat and mass transfer or optimise fluid mixing. These properties make them essential in applications such as

© The Author(s), 2025. Published by Cambridge University Press. This is an Open Access article, distributed under the terms of the Creative Commons Attribution licence (https://creativecommons.org/licenses/by/4.0/), which permits unrestricted re-use, distribution and reproduction, provided the original article is properly cited.

https://doi.org/10.1017/flo.2025.10036 Published online by Cambridge University Press

filtration, catalysis (Lucci et al., 2017) or heat exchangers (Rashidi et al., 2019). In turbulent combustion systems, porous media contribute to ultra-low emission technologies, such as heterogeneous combustion (Trimis & Durst, 1996; Wood & Harris, 2008, Boigné et al., 2019), by improving mixing and stabilising flames.

Furthermore, porous media are widely studied for noise attenuation in aeronautical applications, such as liners in engine nacelle (Ma & Su, 2020) and trailing edges of airfoils (Teruna et al., 2020). However, their intricate flow dynamics, particularly at high Reynolds numbers, presents significant experimental and computational challenges (Wood et al., 2020; Jin & Kuznetsov, 2024).

Despite the widespread use of porous media, their geometric complexity and specific physical behaviours in turbulent flows make accurate numerical simulations challenging, even with high performance computing. Experimental studies are all the more difficult due to limited optical access to the pore structures, which hinders direct observations without disturbing the natural flow. As a result, many historical studies have focused on laminar flow regimes and simplified geometries, such as packed spheres or two-dimensional (2-D) porous structures made of circular or squared cylinders, especially through numerical approaches (Jin et al., 2017; Srikanth et al., 2021; Rao & Jin, 2022). While several macroscopic models have been proposed, as reviewed by Jin and Kuznetsov (2024), present understanding of turbulence in porous media remains limited due to the lack of high-fidelity data, which hinders the development of *ad hoc* turbulence models.

Modelling in porous media typically relies on macroscopic equations, derived via time, volume or combined averaging of the microscopic governing equations, leading to the RANS (Reynolds-averaged Navier–Stokes (NS)), VANS (volume-averaged NS) and DANS (double-averaged NS) equations. Initial approaches employed traditional RANS models, such as the κ-ε (Kuwahara et al., 1998) or v^2-f models (Kazerooni & Hannani, 2007), where κ is the turbulent kinetic energy, ε is its dissipation rate, $v^2 \equiv v'^2$ is the squared wall-normal velocity fluctuation, and f is the elliptic-relaxation function accounting for pressure-strain redistribution. Jin et al. (2015) examined flows in rough-walled channels, where the walls were covered with porous elements, using eight classical RANS models and compared the results with direct numerical simulations (DNSs) data. Their findings revealed errors exceeding 20% in the friction coefficient predictions across all examined models, demonstrating that first- and second-order RANS models could yield incorrect trends.

Consequently, significant efforts have been devoted to developing turbulence models tailored for porous media, particularly in the turbulent regime. The prevailing approach employs the DANS equations with a two-equation κ-ε model closure, introducing an effective viscosity through the Boussinesq hypothesis (Masuoka & Takatsu, 1996; Pedras & de Lemos, 2003; de Lemos, 2005; Nakayama & Kuwahara, 2008). However, these models have two key limitations. First, their coefficients are typically calibrated for specific applications (e.g. periodic cells at moderate Reynolds numbers), restricting their general character; second, they rely on strong closure assumptions, such as isotropy, which can introduce inaccuracies and uncertainties, particularly in complex porous wall systems where anisotropy is dominant (de Lemos, 2012). Developing a turbulence model requires balancing accuracy and efficiency, which demands a fundamental understanding of turbulence, supported by high-fidelity experiments or numerical simulations like pore-resolved DNS

Recent advances in computational resources and high performance computing have enabled more advanced and detailed numerical studies of simplified porous media, such as periodically arranged cylinders or spheres, in transitional and fully turbulent regimes (see the review by Wood 2020). These advancements provide an opportunity to better understand the physics of the flow inside porous media and refine turbulence models for improved accuracy and broader applicability (Jin & Kuznetsov, 2024). Simulations such as DNS and large eddy simulation (LES) of porous medium flows are typically performed using the finite volume method (FVM) (Jin et al., 2015, Gasow et al., 2020, 2021, 2022; Wang et al., 2021, 2022; Srikanth et al., 2021) or the lattice Boltzmann method (LBM) (Suga, 2016; Jin et al., 2017; He et al., 2018, 2019; Liu et al., 2021, 2023; Diao et al., 2023). Finite difference and spectral methods are less commonly employed in this context. Among these techniques, LBM has gained popularity due to its parallelisability. However, further research is required to enhance LBM's

https://doi.org/10.1017/flo.2025.10036 Published online by Cambridge University Press

applicability, particularly regarding numerical stability and its extension to compressible flows (Fattahi et al., 2016).

Commonly, DNS and LES employ body-fitted approaches that suffer from strong CPU limitation due to the no-slip boundary conditions (Jin et al., 2015). A key challenge in simulating porous media is the fine resolution required, which, along with body-fitted meshing constraints, increases computational costs. Mesh-related issues, such as poor-quality cells at contact regions, can be addressed with Cartesian grid-based methods like immersed boundary conditions (IBCs) (Mittal & Iaccarino, 2005) and LBM.

In this context, a critical gap persists in understanding the interaction between turbulent flows and complex porous geometries, particularly in applications involving combustion. Addressing this challenge requires the development of advanced numerical techniques capable of accurately capturing the dynamics between turbulent flows and porous media. In the present work, we propose a high-fidelity numerical approach to investigate such interactions. A spectral difference (SD) method-based solver for the compressible NS equations, coupled with IBCs and pressure gradient scaling (PGS), is used to perform DNSs. These enhancements significantly improve both the accuracy and computational efficiency of the simulations, thereby enabling a deeper understanding of turbulence–porous medium interactions under realistic engineering conditions.

This study evaluates the robustness and reliability of the proposed numerical framework (Section 2), through benchmark tests described in Section 3. First, the implementation of IBCs within the SDM solver is compared with the classical body-fitted approach (Section 3.1). Second, the influence of the PGS method is assessed (Section 3.2). Afterwards, the full solver is benchmarked against the FVM-DNS data from Jin et al. (2015) in Section 3.3, ensuring consistency with high-fidelity reference data and confirming its suitability for simulating turbulent flows in porous geometries. Finally, an application case on a complex porous medium geometry is provided in Section 4 and conclusions are drawn in Section 5.

2. Numerical methodology

This study uses the JAGUAR code (ONERA–CERFACS ©) to perform DNSs, relying on an SD method to solve the unsteady compressible NS equations on unstructured grids (Cassagne et al., 2015; Vanharen et al., 2017; Veilleux et al., 2022). The code employs a nodal, polynomial-based spectral representation of order p, in combination with advanced time integration techniques and Riemann solvers for flux reconstruction (Marchal et al., 2023). Regarding spatial discretisation, the solver uses Lagrange polynomials of order p to represent cell solutions and quadrature-based interpolation for flux computations. In this study $p = 4$ is adopted. Solution points are distributed according to Gauss–Chebyshev nodes of the first kind, yielding $(p+1)^3$ points per cell, while flux points follow Gauss–Legendre quadrature, providing $(p+2)^3$ points per cell, ensuring high-order accuracy. Diffusion terms are treated following the classical approach of Kopriva (1998), without p-refinement. Inter-element numerical fluxes are computed using the Harten–Lax–van Leer–contact Riemann solver (Toro, 2009, pp. 315–344). Temporal discretisation is performed via the explicit five-stage, fourth-order total variation diminishing Runge–Kutta scheme of Spiteri and Ruuth (2002), which offers a favourable trade-off between computational efficiency and stability. A Courant–Friedrichs–Lewy (CFL) number of 0.15 is used in all simulations, and adaptive time stepping ensures numerical stability throughout the simulations. The PGS method is available (Section 2.1). Concerning the boundary conditions, IBCs are adopted (Section 2.2) and the possibility of injecting turbulence at the inlet is implemented via the synthetic random Fourier mode (SRFM) method based on a von Kármán-Pao (VKP) energy spectrum (Section 2.3).

2.1. Pressure gradient scaling

The method aims to improve the computational efficiency of low-Mach-number simulations performed with a compressible NS solver using explicit time integration schemes (Ramshaw et al., 1985). It introduces a scaling coefficient $\alpha > 1$ applied to the pressure p, such that $p_{\mathrm{PGS}} = p_{\mathrm{noPGS}}/\alpha^2$, which reduces

https://doi.org/10.1017/flo.2025.10036 Published online by Cambridge University Press

the effective speed of sound $c = \sqrt{\gamma p/\rho}$ by a factor $1/\alpha$, where $\gamma = C_p/C_v$ is the ratio of specific heats, with C_p the specific heat at constant pressure and C_v the specific heat at constant volume, and ρ is the fluid density. As a result, the CFL constraint on the time step, $\Delta t = \mathrm{CFL} \cdot \Delta x/(c + |\vec{u}|)$, where Δx is the minimum mesh size, $\vec{u}$ is the velocity vector and CFL is chosen to ensure stability without preconditioning, is relaxed. Hence, the maximum admissible time step increases by a factor α, i.e. $\Delta t_{\mathrm{PGS}} = \alpha\, \Delta t_{\mathrm{noPGS}}$. Physically, this corresponds to reducing the sensitivity of the momentum equation to pressure gradients while preserving the velocity field, provided that pressure inhomogeneities remain small. It can also be interpreted as an 'artificial increase of compressibility', since the effective Mach number $Ma = |\vec{u}|/c$ is augmented by a factor α due to the reduced sound speed.

Mathematically, let us consider a decomposition of the pressure field into a spatially averaged component and a fluctuation term, $p(\vec{x},t) = \bar{p}(t) + p'(\vec{x},t)$. If the condition $p'/\bar{p} \ll 1$ holds, one may choose α such that $\alpha^2 p'/\bar{p} \ll 1$. Under this assumption, the pressure gradient term in the momentum equation can be approximated as $\nabla p \simeq \nabla(\hat{p}/\alpha^2)$, with $\hat{p} = \bar{p} + \alpha^2 p'$, where $\hat{p}$ is referred to as the 'modified pressure field' in the PGS framework. Therefore, the pressure-gradient-scaled compressible NS equations in conservative form read

$$\begin{cases} \partial_t \rho + \vec{\nabla} \cdot (\rho \vec{u}) & = 0, \\ \partial_t (\rho \vec{u}) + \vec{\nabla} \cdot (\rho \vec{u} \otimes \vec{u}) & = -1/\alpha^2 \vec{\nabla} \hat{p} + \vec{\nabla} \cdot \bar{\bar{\tau}} + \vec{f}, \\ \partial_t (\rho E) + \vec{\nabla} \cdot (\vec{u}(\rho E + \hat{p})) & = \vec{\nabla} \cdot \left(\vec{u}\, \bar{\bar{\tau}} + \lambda \vec{\nabla} \hat{T} \right), \end{cases} \tag{2.1}$$

where $E = e + \frac{1}{2}|\vec{u}|^2$ is the total energy per unit mass, $\bar{\bar{\tau}} = \mu(\vec{\nabla}\vec{u} + \vec{\nabla}\vec{u}^T) - \frac{2}{3}\mu \vec{\nabla} \cdot \vec{u}\, \bar{\bar{I}}$ is the shear stress tensor, μ is the dynamic viscosity, $\lambda = C_p \mu/Pr$ is the thermal conductivity, C_p is the specific heat at constant pressure, Pr is the Prandtl number, $\vec{f}$ represents the source term accounting for external or artificial forces and $\hat{T} = f(\hat{p}, \rho)$ is the temperature, which follows the state equation based on the modified pressure $\hat{p}(\mathbf{x},t)$. Note that the PGS equations (2.1) maintain the same formal structure as the classical compressible NS equations but with a modified pressure field.

2.2. Immersed boundary conditions

The IBCs are implemented in JAGUAR code (D'Ayer et al., 2025) via the Brinkman penalisation method (Liu & Vasilyev, 2007), and integrated using the Strang splitting approach, as described by MacNamara and Strang (2016). This approach belongs to the family of volume penalisation (VP) methods (Arquis & Caltagirone, 1984), and is thus classified as a continuous immersed boundary method (IBM). Hereafter, we will use the term IBC to refer specifically to the IBM implementation employed in this work.

A time-independent mask function $\chi(\vec{x}) = \{1 \text{ if } \vec{x} \in \Omega,\ 0 \text{ if } \vec{x} \in \mathcal{F}\}$ distinguishes the fluid domain $\mathcal{F}$ from the solid regions Ω. A VP source term is added to the NS equations (2.1) everywhere in the domain to enforce the no-slip and no-penetration conditions at the fluid–solid interface

$$\mathbf{S}(\vec{x},t) = -\chi(\vec{x})/\eta\ \{\vec{0},\ \rho \vec{u_\Omega}(\vec{x},t) - \rho \vec{u}(\vec{x},t),\ \rho E_\Omega(\vec{x},t) - \rho E(\vec{x},t)\}, \tag{2.2}$$

where $\vec{u}_\Omega(\vec{x},t)$ and $E_\Omega(\vec{x},t)$ are the target velocity and total energy at position $\vec{x}$. In practice, the source term is applied only in the solid region ($\chi = 1$) and the target velocity is set to zero, $\vec{u_\Omega}(\vec{x},t) = \vec{0}$, so that the total energy reduces to the internal energy and a target temperature $T_\Omega(\vec{x},t)$ can be introduced for a calorically perfect gas: $E_\Omega = e_\Omega = c_v T_\Omega$, where c_v is the specific heat at constant volume of the fluid. In this work, the walls are assumed to be isothermal with the inlet temperature so that $T_\Omega = T_0 = 300$ K. A crucial role in the continuous VP approach is played by the Brinkman penalisation coefficient η, which acts as a normalised viscous permeability ($0 < \eta \ll 1$). This coefficient controls the effectiveness of the method at the fluid–solid interface: decreasing η sharpens the diffuse representation of this interface where the velocity is very small but not zero and whose exact position is not known *a priori*. In fact, the error associated with this approach can be expressed as $\|\vec{u} - \vec{u}_\eta^{[n]}\| \le \|\vec{u} - \vec{u}_\eta\| + \|\vec{u}_\eta - \vec{u}_\eta^{[n]}\|$, where $\vec{u}$ is the exact solution of the NS equations, $\vec{u}_\eta$ is the theoretical solution obtained using the VP-NS approach and $\vec{u}_\eta^{[n]}$ is the corresponding numerical solution. It is known that $\|\vec{u} - \vec{u}_\eta\| = O(\eta^{-1/2})$ decays

https://doi.org/10.1017/flo.2025.10036 Published online by Cambridge University Press

exponentially with η (D'Ayer et al., 2025); thus, at the wall, we expect $\vec{u}_\eta \sim O(\eta^{-1/2})$. However, the discretisation error $\|\vec{u}_\eta - \vec{u}_\eta^{[n]}\|$ may also depend on η. It is evident that small values of η are desirable, as they enforce the boundary conditions more accurately. However, decreasing η increases the system stiffness, and an explicit treatment of the penalisation term imposes a severe time-step restriction, $\Delta t \leq \eta$, for numerical stability (Kolomenskiy & Schneider, 2009). To circumvent this limitation, the penalisation term is treated separately from the other NS terms using Strang splitting (MacNamara & Strang, 2016).

In the present computations, η is set to 10^{-10}, several orders smaller than the time step, ensuring stability and effective boundary-condition enforcement. This yields normalised velocities in the diffuse interface of 10^{-5}–10^{-7}, consistent with the theoretical prediction $\vec{u}_\eta \sim O(\eta^{-1/2}) = O(10^{-5})$.

Mesh resolution is also critical for accuracy. While refinement generally helps, the relative position of cells to the boundary matters: partially immersed cells can cause spurious near-wall fluctuations (Runge phenomena) since fixed-degree polynomials poorly approximate discontinuities (D'Ayer et al., 2025, p. 6). Still, with $\eta \ll 1$, a sufficiently fine mesh gives results close to body-fitted simulations, as shown by D'Ayer et al. (2025) for cylinder and rough-channel flows.

2.3. Synthetic turbulence injection

The turbulent velocity field at the inlet, $\vec{u}_{in} = \vec{\bar{u}}_{in} + \vec{u}'_{in}$, is modelled using Reynolds decomposition, where $\vec{\bar{u}}_{in}$ is the time-averaged velocity and $\vec{u}'_{in}$ represents turbulent fluctuations. The mean velocity $\vec{\bar{u}}_{in}$ is prescribed according to the desired profile, while $\vec{u}'_{in}$ is injected using the SRFM (Marchal et al., 2023). The method generates homogeneous isotropic turbulence by summing N Fourier modes with wavenumbers κ_n, following a user-defined energy spectrum. In this study, we use a VKP energy spectrum, detailed in Appendix C, with $N = 300$, turbulence intensity $\mathrm{Tu} = u'_{rms}/\bar{u}_{in} = 10\%$, energy-containing length scales $L_{e,\max} = 0.66$ m, and Kolmogorov length scales $\eta_k = (\kappa_{Kol}^{-1}) = 6.33 \times 10^{-3}$ m. It should be emphasised that the applied boundary condition is not inherently periodic and therefore does not preserve perfect inlet periodicity under periodic boundary conditions.

3. Benchmark tests

3.1. The IBC validation

To validate the effectiveness of IBCs in modelling solid walls within complex geometries, we perform DNS of flow through a high-porosity periodic 2-D porous medium. The results obtained using IBCs are compared with those obtained with a traditional body-fitted meshing. The test geometry comprises square-edged obstacles, a particularly challenging case for IBCs due to the sharp fluid–solid interfaces.

Note that the compressible NS equations solved (2.1) include the energy equation. However, no heat transfer tests were performed for the configurations considered, since the present work focuses on velocity and turbulence statistics. Relevant validations of our IBC approach, also for heat transfer, are provided in D'Ayer et al. (2025) for a flow past a circular cylinder and a heated channel with academic roughness.

3.1.1. Numerical set-up

A turbulent flow past a squared cylinder (Figure 1 a) at Reynolds number $Re = u_m d/\nu = 1200$ is considered, where the kinematic viscosity is $\nu = 1.33 \times 10^{-3}$ m^{2}s^{-1}, the square size is $d = 0.05$ m and the mean velocity component along the x_1-axis is $u_m = 32.0$ ms^{-1}. The flow is driven by a source term $\vec{f} = \{g_1, 0, 0\}$ in the NS equations (2.1), with $g_1 = 1500$ Pa/m in both simulations, consistent with Section 3.3. The relatively high Reynolds number ensures conservative validation of the IBC approach. Periodic boundary conditions are imposed in all directions, yielding an effective porosity $\varphi = 0.93$, with a computational domain $(L_x \times L_y \times L_z) = (5d \times 3d \times 4d)$. The IBC case uses a Cartesian grid with $(N_x \times N_y \times N_z) = (60 \times 36 \times 30)$ hexahedral cells and SD polynomial order $p = 4$, giving approximately

https://doi.org/10.1017/flo.2025.10036 Published online by Cambridge University Press

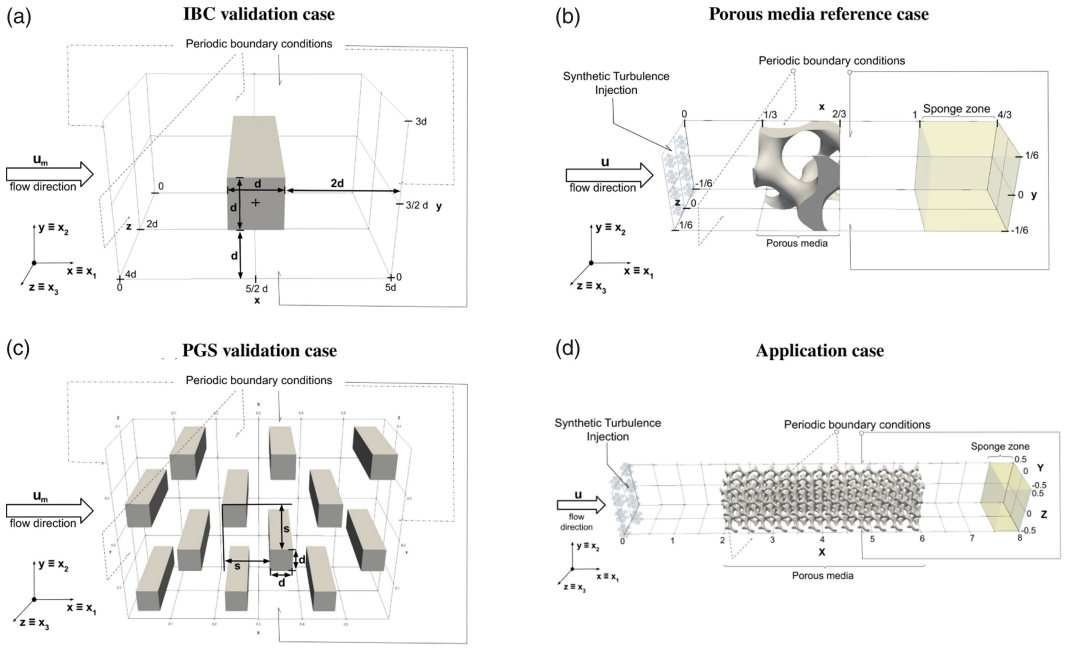


Figure 1. *Computational domain configurations and geometries used in the study.*

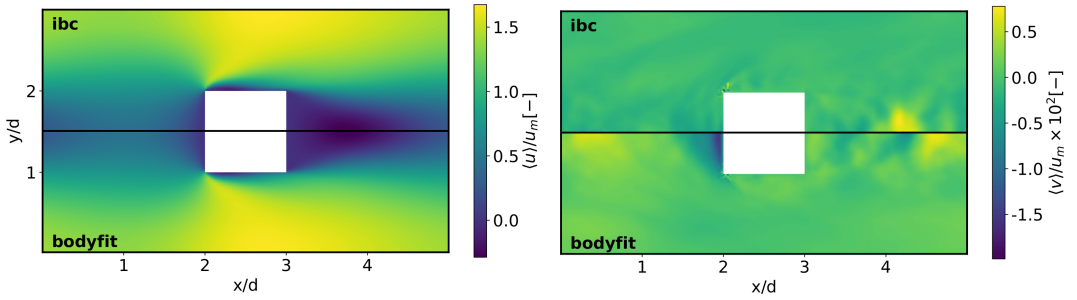


Figure 2. *The IBC validation: first-order velocity statistics $\langle u_i \rangle$ on the averaged longitudinal plane (x_1, x_2).*

8.1 million degrees of freedom (DoF), consistent with Jin et al. (2015) for $Re = 1000$. The body-fitted case employs the same grid with the solid volume removed, yielding 7.6 million DoF. Average resolutions are $(\Delta x_1/d)_{avg} = (\Delta x_2/d)_{avg} = 1.7 \times 10^{-2}$ and $(\Delta x_3/d)_{avg} = 2.7 \times 10^{-2}$.

Solver details are provided in Section 2. To isolate boundary-condition effects, no PGS method was used. Simulations ran on the IRENE Skylake Partition at TGCC with 500 processors for approximately 25 000 CPU hours, advanced until statistical values such as $\langle u \rangle$ and $\langle uu \rangle$ stabilised. This required ~10 wash-out cycles at $p = 4$ after initialising at lower resolution, where a wash-out cycle corresponds to the mean flow traversal time $T_{\text{char}} = 5d/u_m \approx 1.35 \times 10^{-2}$ s. The time step from the CFL condition was $\Delta t = 3.8 \times 10^{-7}$ s in both cases.

3.1.2. Mean velocity field

In Figure 2, the 2-D distributions of the mean velocity field components $\langle u_i \rangle$ over the averaged longitudinal plane (x_1, x_2) are presented. Since the volume average of $\langle w \rangle$ is theoretically zero due to the 2-D

https://doi.org/10.1017/flo.2025.10036 Published online by Cambridge University Press

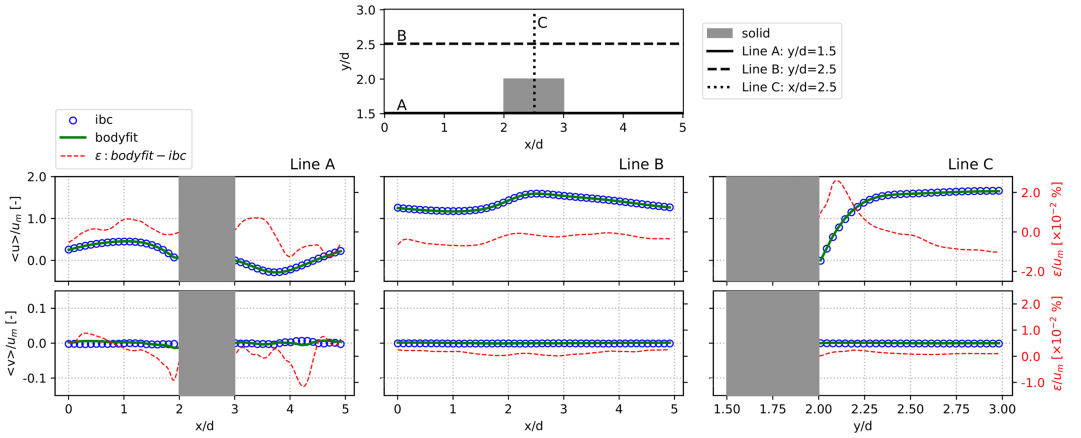


Figure 3. *The IBC validation: $\langle u_i \rangle$ on lines along x_1 and x_2 from the averaged longitudinal plane (x_1,x_2). For visualisation, IBC results are shown at reduced resolution; however, both body-fitted results and the error between the methods are presented at full simulation resolution.*

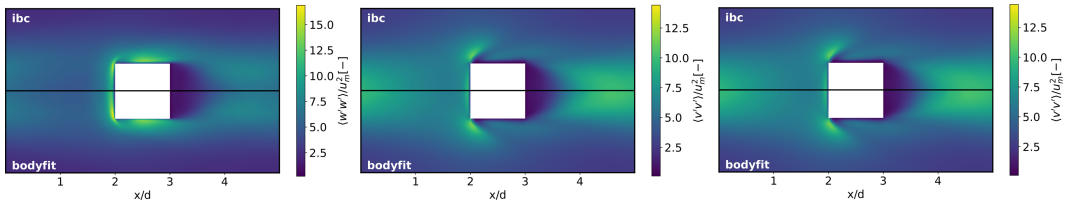


Figure 4. *The IBC validation: second-order velocity statistics $\langle u_i' u_i' \rangle$ on the averaged longitudinal plane (x_1,x_2).*

configuration, this component is not shown. The streamwise velocity component, $\langle u \rangle$, exhibits excellent agreement, particularly in the critical square edge region (more details in Appendix A), where the boundary layer (BL) originates. The cross-wise component, $\langle v \rangle$, shows slight discrepancies, particularly in the impingement and wake regions. The differences in the impingement zone are expected, because the IBCs model the wall as a permeable medium, preventing the velocity from dropping abruptly to zero as it would under a no-slip condition. In the wake region, we attribute the observed discrepancies to the lower dissipation of IBCs compared with body-fitted approaches. Since IBCs represent the solid boundary as a low permeability medium, they capture weaker velocity gradients at the wall, which directly affects the computation of dissipation. As a result, IBCs tend to slightly underestimate the velocity magnitude, as they do not fully account for all dissipation mechanisms at the wall. The majority of the observed error occurs in the wake region due to a combination of slightly different upstream conditions that can amplify the upstream–downstream wake interactions in a periodic configuration.

To quantify these effects, Figure 3 shows velocity profiles along the x_1 and x_2-directions, confirming nearly perfect agreement for $\langle u \rangle$ and only minor, localised discrepancies in $\langle v \rangle$. Figure 4 presents the Reynolds stress tensor (RST) components $\langle u_i' u_i' \rangle$ on the (x_1, x_2) plane, showing excellent agreement in both shape and magnitude, even near walls. Table 1 summarises volume-averaged errors for first- and second-order velocity statistics, with all L_2 and L_∞ norms below 1% and 5.5%, respectively.

3.2. The PGS validation

While the efficacy of PGS has been demonstrated by various authors for FVM solvers (Papageorgakis & Assanis, 1999), its performance within an SD solver using IBCs for complex geometries has yet to be thoroughly assessed. The objective of this validation is, therefore, to compare two simulations of a

https://doi.org/10.1017/flo.2025.10036 Published online by Cambridge University Press

Table 1. *The IBC validation: volume-averaged errors using different norms (L_1, L_2 and L_∞) for first- and second-order velocity statistics. Norms are normalised by the bulk velocity u_m of the body-fitted case*

	$\langle u \rangle$	$\langle v \rangle$	$\langle u'u' \rangle$	$\langle v'v' \rangle$	$\langle w'w' \rangle$	$\langle u'v' \rangle$	$\langle u'w' \rangle$	$\langle v'w' \rangle$
L_1 [%]	0.80	0.20	0.66	0.21	0.18	0.19	0.10	0.06
L_2 [%]	0.96	0.27	0.76	0.29	0.31	0.21	0.13	0.08
L_∞ [%]	5.58	1.54	5.46	4.99	3.83	1.00	0.74	0.27

porous medium using both PGS and non-PGS approaches. To ensure a fair comparison, both simulations are conducted over the same physical time span. However, the non-PGS case requires significantly more iterations. Since PGS modifies the flow dynamics by artificially adjusting the pressure field, allowing for a relaxed time step via an increased Mach number, the critical concern is whether this method alters the mean flow or fails to capture the full spectrum of temporal frequencies required for statistical analysis.

3.2.1. Numerical set-up

We consider a simplified porous medium configuration as shown in Figure 1b. This set-up models a turbulent flow through a single pore of a Gyroid-type porous topology, belonging to the triply periodic minimal surface (TPMS) family (Wang et al., 2023), whose solid structure is defined by positive values of the function: $f(x,y,z) = \sin(k_x x)\cos(k_y y) + \sin(k_y y)\cos(k_z z) + \sin(k_z z)\cos(k_x x) - \sigma_t$. In this case the structural factor $\sigma_t = 0.75$, meaning a porosity $\varphi = 0.7$, with wavenumber coefficients $k_x = k_y = k_z = 6\pi\ \mathrm{m}^{-1}$. The computational domain is a hexahedral box $(L_x \times L_y \times L_z) = (4s \times s \times s)$, where a cubic pore cell of dimension $s = 1/3$ m is located within the region $x \in [s, 2s]$. Periodic boundary conditions are applied in the directions transverse to the flow. A turbulent flow is injected at the inlet along the flow direction with a unity mean axial velocity $u_0 = 1\ \mathrm{ms}^{-1}$, a Reynolds number $Re = (3s)u_0/\nu = 2500$ and a turbulent VKP spectrum, described in Section 2.3. A sponge zone is implemented just before the outlet ($x \in [3s, 4s]$) to prevent acoustic wave reflections. A pressure outlet condition is imposed with a reference pressure $p_0 = 10^5$ Pa. Both simulations employ IBCs on a Cartesian grid with $(N_x \times N_y \times N_z) = (80 \times 20 \times 20)$ hexahedral cells, using a SD polynomial order $p = 4$, resulting in approximately 4 million DoFs. This grid resolution is selected to ensure a ratio of $\eta_k/\Delta x_{\mathrm{avg}} = 1.5$ (Pope, 2000, pp. 344–351), where η_k is the injected Kolmogorov length scale.

Two simulations were performed: one with PGS ($1/\alpha^2 = 0.05$) and one without. The average time steps were 6.2×10^{-6} and 1.4×10^{-6} s, respectively. Low-pressure inhomogeneity assumptions were confirmed, with negligible overall pressure gradients. Simulations ran on the Skylake partition of the IRENE supercomputer at TGCC using 512 processors, requiring 30 000 CPU hours with PGS and 125 000 hours without. They continued until statistical quantities, such as time correlations, reached steady state – approximately 20 wash-out cycles, after an initial ramp-up of SD polynomial order and PGS influence. A representative period of over 10 wash-out cycles ($T_{\text{wash-out}} = (L_x - L_{x,\text{sponge}})/u_0 = 1$ s) was selected for robust statistics. The PGS simulation also served to initialise the no-PGS case, providing approximate initial conditions for high-fidelity computations.

It is important to note that the time step in our simulations is constrained by the combined effect of the CFL condition and the high spatial resolution required for accurately modelling complex geometries, rather than by the physical time scales of turbulence. Specifically, the estimated Kolmogorov time scale τ_η in homogeneous isotropic turbulence (HIT) conditions (Pope, 2000, p. 185) of the injected turbulent spectrum is of the order of 10^{-2} s. In contrast, the simulation time steps are of the order of 1.0×10^{-6} s (for a CFL = 0.15), nearly four orders of magnitude smaller. As a result, the simulations resolve extremely high frequencies that are not only unnecessary for our analysis but also computationally expensive. This highlights the importance of validating the PGS method.

https://doi.org/10.1017/flo.2025.10036 Published online by Cambridge University Press

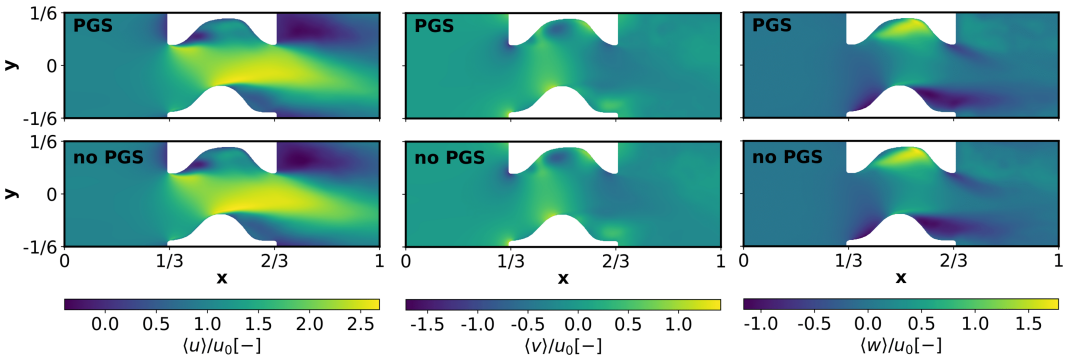


Figure 5. *The PGS validation: mean velocity components $\langle u_i \rangle / u_0$ on the longitudinal pore-crossing plane.*

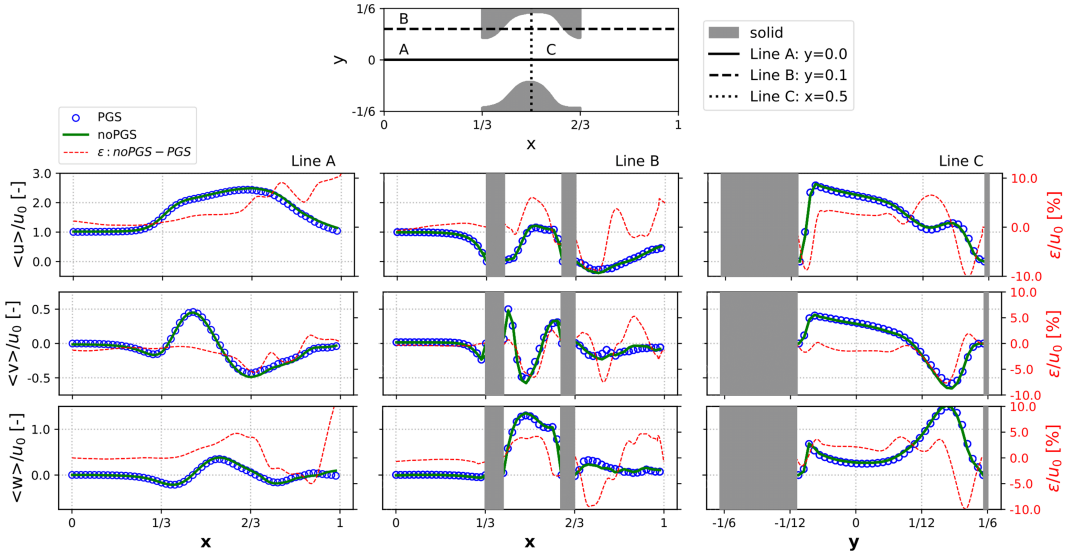


Figure 6. *The PGS validation: $\langle u_i \rangle$ on lines along x and y extracted from the longitudinal pore-crossing plane. For visualisation, PGS results are shown at reduced resolution; however, both no PGS results and the error between the methods are presented at full simulation resolution.*

3.2.2. Mean velocity field

In Figure 5, the mean velocity components $\langle u_i(\vec{x}_0, t) \rangle$ in the streamwise longitudinal pore-crossing section (x, y) are analysed. Good agreement is observed between the PGS and no-PGS approaches in both the shape and magnitude of the velocity field. Local minima and maxima are also reasonably well predicted, and detachment phenomena and wake structures remain consistent. To better quantify the differences, velocity profiles along the x- and y-axes are extracted from Figure 5 and shown in Figure 6. The PGS approach effectively captures the mean flow features, with only minor accuracy losses in separation and shear regions, where local relative errors may reach up to 10%. These discrepancies likely arise from a slight shift in the inlet–outlet pressure drop induced by the PGS, which appears to cause a mild suction effect at the inlet, slightly advancing wake development. Notably, PGS performs relatively well near the walls, suggesting that any potential PGS–IBC interaction does not significantly amplify the errors introduced by IBCs.

Table 2 presents volume-averaged errors for both first and second-order velocity statistics using different norms to compare PGS and no-PGS simulations. The mean relative errors in norm L_2 are all below

https://doi.org/10.1017/flo.2025.10036 Published online by Cambridge University Press

Table 2. *The PGS validation: volume-averaged errors using different norms (L_1, L_2 and L_∞) for first- and second-order velocity field statistics, averaged over the computational domain (excluding the sponge zone and the very close region to it)*

	$\langle u \rangle$	$\langle v \rangle$	$\langle w \rangle$	$\langle u'u' \rangle$	$\langle v'v' \rangle$	$\langle w'w' \rangle$	$\langle u'v' \rangle$	$\langle u'w' \rangle$	$\langle v'w' \rangle$
L_1 [%]	2.58	1.84	2.30	1.52	1.42	1.24	0.78	0.84	0.77
L_2 [%]	4.12	2.94	3.99	3.04	2.79	2.42	1.57	1.57	1.47
L_∞ [%]	23.31	27.52	22.24	18.14	19.81	16.34	9.82	8.45	9.16

4.5% and 3.5% for the velocity components $\langle u_i \rangle$ and RST components $\langle u_i' u_j' \rangle$, respectively. The largest local errors are concentrated downstream of the pore, in the wake region, as illustrated in Figure 6. This allows us to say that the slight difference in pressure field affects only the wake area, suggesting that the inside pore physics is not contaminated by the PGS method. This is crucial for applications where we aim to simulate multiple pores in the streamwise direction.

3.2.3. Energy spectra

Since PGS primarily affects time resolution, it is natural to compare temporal signals at the same location with and without PGS. Here, energy spectra $E_{ii}(\vec{x_0}, f)$, where f is the temporal frequency, are analysed at two spatial probes: one upstream (A) of the porous medium in $\vec{x}_A = (0.1, 0.0, 0.0)$ and the other downstream (B) in $\vec{x}_B = (0.8, 0.0, 0.0)$. The energy spectra definition is the one used by Pope (2000, pp. 65–73) as the fast fourier transform (FFT) of the (one-point space) two-time covariance $R_{ii}(\vec{x}_0, t') = \langle u_i'(\vec{x}_0, t) u_i'(\vec{x}_0, t + t') \rangle_T$. In Figure 7, energy spectra of the RST normal components E_{ii} are presented and show strong coherence in energy distribution and overall captured energy.

In the PGS case, the larger time step (lower time resolution) leads to a slight overestimation of energy at the inlet. However, the energy cascade remains consistent. At very high frequencies, numerical noise appears at the inlet, but these non-physical scales are negligible since their energy content is several orders of magnitude lower than the injected Kolmogorov-scale frequency ($f_\eta = 1/\tau_\eta \simeq 12.5$ Hz). At the upstream probe, a peak at $f = 3.0$ Hz corresponds to the injected turbulence, where the energy-containing eddies have a characteristic size $l_0 = 0.33$ m and velocity $u_0 = 1$ m/s, yielding a characteristic time $\tau_0 = l_0/u_0 = 0.33$ s and frequency $f = 1/\tau_0 = 3.0$ Hz. Downstream, two key observations arise. First, the energy spectrum is enriched due to turbulence production by the pore, increasing both kinetic energy and the turbulence-scale range at high frequencies. Second, a peak at $f = 5.5$ Hz corresponds to vortex shedding behind the pore, behaving as a blunt body. This frequency aligns with a turbulent Strouhal number $St = fL/U = 0.25$, considering an approximated obstacle diameter of $L \simeq s/10$ and a mean axial velocity at the pore outlet $U \simeq 1.8$ m/s.

Overall, the robustness of the PGS method is confirmed by the minimal differences in captured energy (integral of the spectrum), which remain below 10% at the downstream probe, the most critical location for this case.

3.3. Porous medium reference case

Following the demonstration of the influence of IBCs and PGS method, we now proceed to a comparison of the complete numerical approach, integrating both PGS and IBCs to enhance the SD solver's performance, with a classical FVM solver, which have been extensively employed in the literature. For this comparative analysis, the reference work of Jin et al. (2015), who conducted high-fidelity DNS using both FVM and LBM on a simplified porous medium consisting of an array of squared cylinders, is reproduced.

As those authors demonstrated comparable performances between their numerical approaches, the present analysis will compare our SD solver to the FVM reference case. This choice is also motivated

https://doi.org/10.1017/flo.2025.10036 Published online by Cambridge University Press

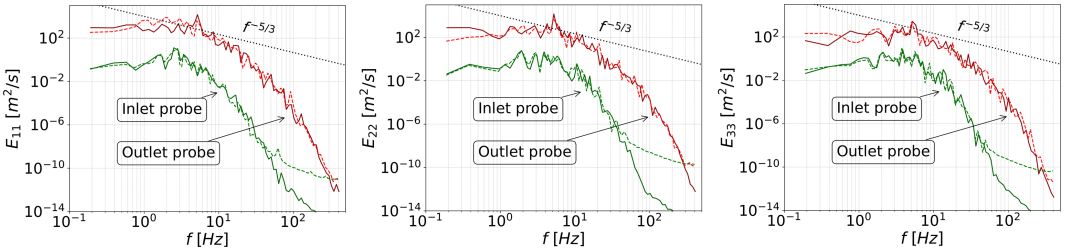


Figure 7. *The PGS validation: comparison of the energy spectra $E_{ii}(\vec{x}, f)$ at the inlet probe location $\vec{x}_A$ (green) and the outlet probe location $\vec{x}_B$ (red). Solid coloured lines (—) correspond to simulations without PGS; dashed coloured lines (- - -) correspond to simulations with PGS; dotted black line (· · ·) represents the Kolmogorov $-5/3$ power law.*

by the FVM's widespread adoption within the porous medium turbulence literature and its generally perceived higher reliability for such complex flows.

The following comparison between SD-DNS and FVM-DNS focuses primarily on two-point velocity correlations, as we are interested in turbulent flow applications.

3.3.1. Numerical set-up

The geometry considered is the one used by Jin et al. (2015), a generic porous medium composed of squared rods of size d arranged periodically to form a porous structure with pore size s (Figure 1c). This geometry has been also used by other authors in their numerical studies (Kuwahara et al., 2006; Suga, 2016; Chu et al., 2018). Specifically, we consider the configuration where $s/d = 2$ (meaning a porosity $\varphi = 0.88$) and $Re = 700$, which corresponds to case E of the high-resolution FVM-DNS simulations presented by Jin et al. (2015).

The size of the computational domain was determined using the concept of REV-T, which defines the representative elementary minimum volume necessary to capture turbulent behaviour without loss of information. Jin et al. (2015) conducted a REV-T size study, systematically reducing the number of bars in the computational domain with periodic boundary conditions until a minimum size was identified that preserved large-scale turbulent structures. Based on their findings, the computational domain is a box of size $(L_x \times L_y \times L_z) = (12d \times 8d \times 4d)$, for a total of 12 squared cylinders of size $d \times d \times 4d$, with $d = 0.05$ m.

Periodic boundary conditions are imposed on all boundaries of the computational domain in all three spatial directions. The turbulent flow analysed is self-generated by the porous medium (Jin et al., 2015) and is imposed by adding a pressure gradient source term in the x_1-direction, as detailed previously in Section 3.1. In this way, a Reynolds number $Re = u_m d/\nu \simeq 700$ is reached, where $u_m = 18.40$ ms^{-1} is the bulk velocity along the x_1-axis. However, we underline that Jin et al. (2015) concluded in their study that the Reynolds number (in the considered range of $500-1000$) has a negligible effect on the dimensionless two-point correlations R_{ii}/u_m^2 for the porosity values being examined.

Moreover, Jin et al. (2015) also performed a mesh convergence study by introducing an accuracy parameter based on dissipation calculations and pressure loss imposed through the pressure gradient source term. Following their approach, we adopted the same mesh density. Using IBCs, this resulted in a Cartesian grid with $(N_x \times N_y \times N_z) = (144 \times 96 \times 30)$ cells and a SD polynomial order of $p = 4$, yielding approximately 51.8 million DoF.

To enhance simulation efficiency, PGS method with a relatively mild value $\alpha^{-2} = 0.7$ is used, allowing for a 20% increase in the time step compared with the case without PGS. We exercise caution when applying PGS in this case because the presence of sharp geometric features can locally induce high Mach numbers, and artificially increasing them through PGS could lead to undesirable effects. However, for smoother geometries, as demonstrated in Section 2.1, more aggressive PGS can be safely employed.

The simulations were conducted on the IRENE Skylake Partition at TGCC using 2500 processors. The total CPU time for the simulation was approximately $150\,000$ h. The simulation was run until

https://doi.org/10.1017/flo.2025.10036 Published online by Cambridge University Press

statistical values, such as spatial correlations, exhibited clear convergence, with time statistics remaining stable. This process required up to 200 wash-out cycles in one pore element. For validation purposes, we do not extend the simulation further to achieve perfect convergence of the two-point correlations, as this process is computationally expensive, especially for the x_3-direction, where convergence is slow. However, we ensure that the observed convergence was sufficient and that the simulated time span of 200 wash-out cycles was comparable to the 250 wash-out cycles performed by Jin et al. (2015), particularly for comparing two-point correlation behaviour. Note that one wash-out cycle is computed considering the characteristic time $T_{\text{char}} = 4d/u_m \simeq 1.1 \times 10^{-2}$ s. The time steps for $p = 4$ are around 3.8×10^{-7} s.

In contrast, Jin et al. (2015) employed a FVM solver that directly solves the incompressible NS equations. Time integration was performed using a second-order implicit backward Euler scheme, while spatial discretisation relied on a second-order central difference method. Pressure–velocity coupling was managed through the pressure-implicit with splitting of operators (PISO) algorithm, and periodic boundary conditions were applied. The simulation used approximately 51.8 million DoFs, with mesh refinement near the walls, and required approximately 50,000 CPU hours (using 480 processors) for the test case considered.

3.3.2. Two-point correlations

One effective approach to detecting turbulent structures and analysing their scales is by determining two-point correlations in the velocity field, as the latter fully characterise an incompressible turbulent flow.

The two-point correlation function between the velocity fluctuations $u_i'(\vec{x_0}, t)$ and $u_j'(\vec{x_0} + \vec{r}, t)$ at a given time t is referred to as the two-point (one-time) autocovariance by Pope (2000, pp. 77–78): $R_{ij}(\vec{r}, \vec{x_0}) = \langle u_i'(\vec{x_0}, t) u_j'(\vec{x_0} + \vec{r}, t) \rangle$. This function characterises how the velocity fluctuations at $\vec{x_0}$ correlate with those at neighbouring points at a distance $\vec{r}$. The peak of this function occurs at $\vec{r} = \vec{0}$, indicating that the strongest correlation is self-referential. Usually, two-point correlation functions are adimensionalised by their peak value $R_{ij}(\vec{r} = \vec{0})$ but here we use instead the bulk velocity squared, as done also by Jin et al. (2015) to remove the influence of the Reynolds number.

Figure 8 presents the 2-D distributions of the normalised two-point correlation functions $R_{11}(\vec{x_0}, \vec{r})/u_m^2$ and $\hat{R}_{11}(\vec{x_0}, \vec{r})/u_m^2$ in the longitudinal midplane. The results closely match the FVM-DNS data of Jin et al., (2015, Figures 4 and 5) in both magnitude and structure. This agreement further confirms the ability of the implemented IBCs to accurately resolve boundary-layer features and the wake dynamics behind the cylinders.

In Figure 9 normalised two-point correlation profiles along the x_1- and x_2-directions are extracted from the planar data of Figure 8. The SD solver accurately predicts both the complex functional behaviour and the peak magnitude of the correlation functions. The same agreement is also found for the turbulent correlation $\hat{R}_{11}/u_m^2$ (Jin et al., 2015, pp. 84–85), not presented here. This implies that both the turbulent and non-turbulent correlation components are faithfully solved. Minor oscillations indicative of incomplete convergence persist, particularly in the x_3-direction. Despite these marginal convergence artefacts, the overall agreement is substantial, with the most significant discrepancy being an approximate 5%–10% underestimation of the $\hat{R}_{11}/u_m^2$ peak. We posit that part of this underestimation would be considerably reduced upon achieving complete convergence of the simulation, as shown by the 90% confidence intervals (CIs). As previously noted, although a trend toward convergence along the x_3-direction was observed, the simulation was stopped due to the high computational cost and time required to reach full convergence, which was considered beyond the primary scope of this validation.

4. Application case

In this section, the whole numerical approach is applied to a complex porous medium (Figure 1d). A turbulent flow through a TPMS porous geometry of the Gyroid type is considered, the geometry

https://doi.org/10.1017/flo.2025.10036 Published online by Cambridge University Press

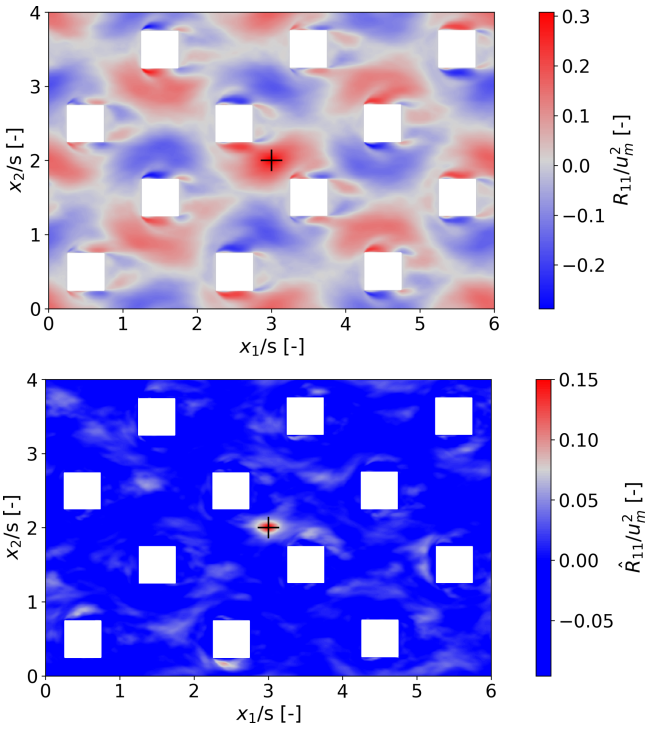


Figure 8. *Two-point correlation $R_{11}(\vec{x_0},\vec{r})/u_m^2$ (top) and turbulent two-point correlation $\hat{R}_{11}(\vec{x_0},\vec{r})/u_m^2$ (bottom) in the plane $x_3 = L_3/2$ at the correlation point $\vec{x_0} = (3s, 2s, s)$, marked with '+'.*

being defined using the equation defined in Section 3.2 with a structural factor $\sigma_t = 1.20$, corresponding to a porosity $\varphi = 0.90$ and $k_x = k_y = k_z = 6\pi$ m^{-1}. The computational domain is a box $(L_x \times L_y \times L_z) = (8L \times L \times L)$, where L is unity. This configuration extends the elementary pore simulation analysed in Section 3.2, using the same boundary conditions set-up and the same inlet Reynolds number $Re = Lu_0/\nu = 2500$. The porous matrix is embedded in the region $x \in [2L, 6L]$ and it accounts for $12 \times 3 \times 3$ pores in the x, y and z directions, respectively, with a pore cell size $s = L/3$. A sponge zone is implemented in the region $x \in [7.5L, 8L]$, sufficiently far from the porous matrix to avoid interaction with the wakes immediately downstream.

The simulation employs IBCs on a Cartesian grid of $(N_x \times N_y \times N_z) = (480 \times 60 \times 60)$ hexahedral cells with SD polynomial order $p = 4$, yielding ~216 million DoF (~1 million per pore cell). The resolution satisfies $\eta_\kappa/\Delta x_{\text{avg}} = 1.5$ (Pope, 2000), with $\eta_\kappa = 6.33 \times 10^{-3}$ m. Mesh refinement confirmed convergence, and a domain size study (configurations 3×3 vs. 5×5 pores) showed no significant differences in two-point correlations, so the 3×3 set-up was adopted.

The PGS method uses $1/\alpha^2 = 0.05$, allowing a much $\alpha \simeq 4.5$ times larger time step than the baseline (1.95×10^{-6} s). Runs were performed on the IRENE Skylake partition with 3500 processors at a cost of ~2 million CPU hours. Statistics stabilised after approximately 60 wash-out cycles ($T_{\text{wash-out}} = s/u_0 = 0.33$ s). A representative window of ~100 wash-out cycles was then used to collect robust turbulence data.

4.1. Preliminary results

Our primary interest lies in the investigation of turbulent flow behaviour in porous media, particularly in the context of turbulent combustion applications. A key focus is understanding the evolution of turbulent length scales as the flow develops within the porous matrix. Figure 10 presents the vorticity

https://doi.org/10.1017/flo.2025.10036 Published online by Cambridge University Press

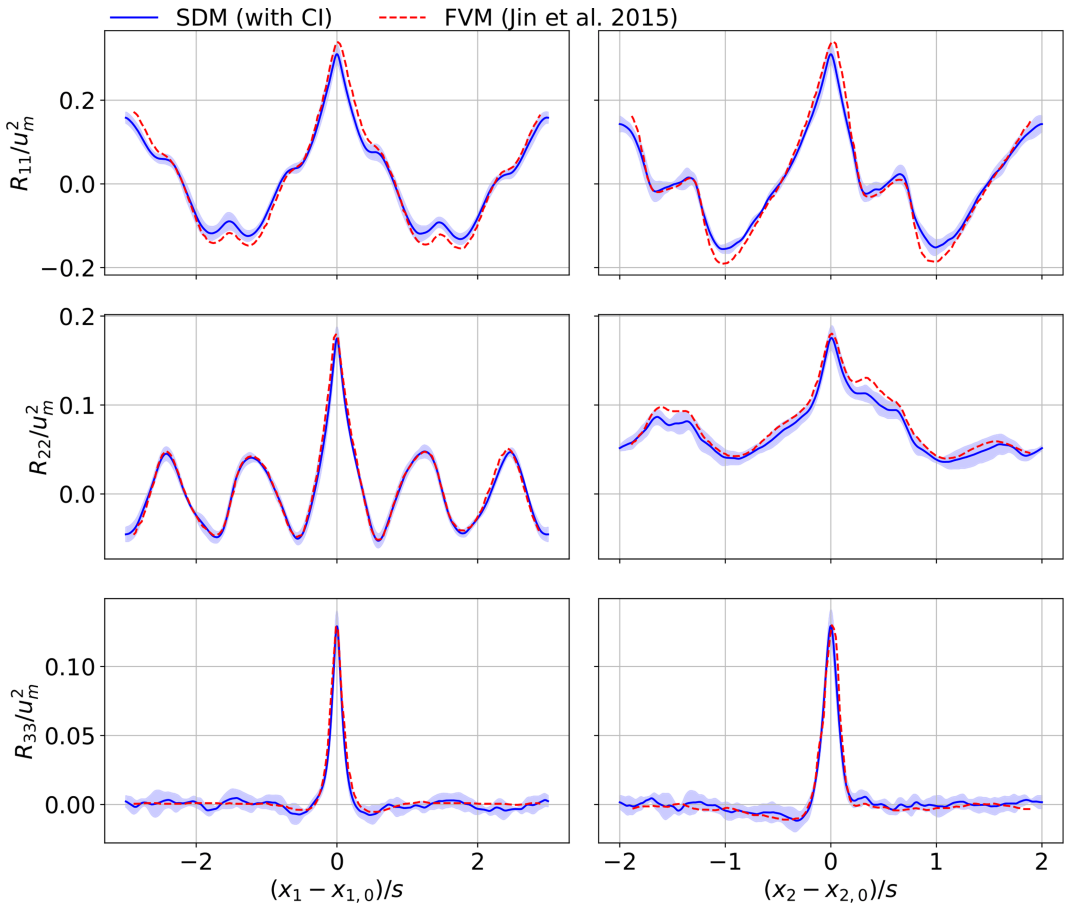


Figure 9. *Two-point correlations $R_{ij}(\vec{x_0}, \vec{r})/u_m^2$ at the correlation point $\vec{x_0} = (3s, 2s, s)$ along x_1-axis (left) and x_2-axis (right). — (blue) indicates the SD results with a 90% CI region highlighted; - - - (red) indicates FVM results of Jin et al. (2015).*

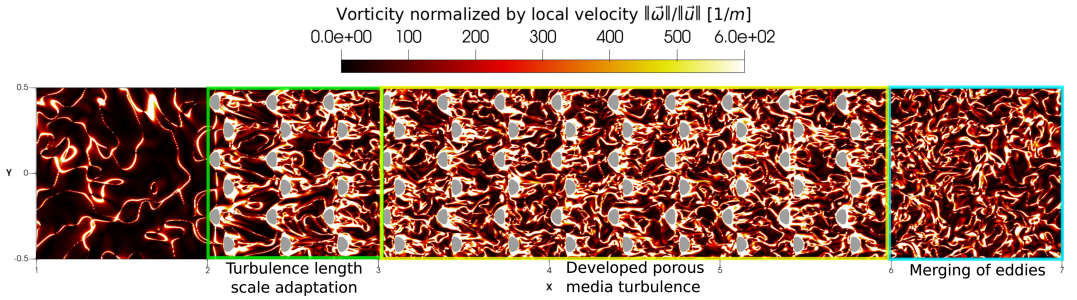


Figure 10. *Vorticity magnitude normalised by the local velocity magnitude $\|\vec{\omega}\|/\|\vec{u}\|$.*

magnitude normalised by the local velocity magnitude, visualised on a longitudinal plane. This highlights the characteristic eddy sizes along the streamwise direction. At the inlet, the imposed turbulence contains energy-bearing eddies with characteristic dimensions approximately twice the pore cell size. As the flow enters the porous structure, these eddies undergo a progressive scale reduction, adapting to the pore size over several layers in the longitudinal direction. We refer to this region as the turbulence length scale adaptation region, which is of practical importance. In combustion applications, this

https://doi.org/10.1017/flo.2025.10036 Published online by Cambridge University Press

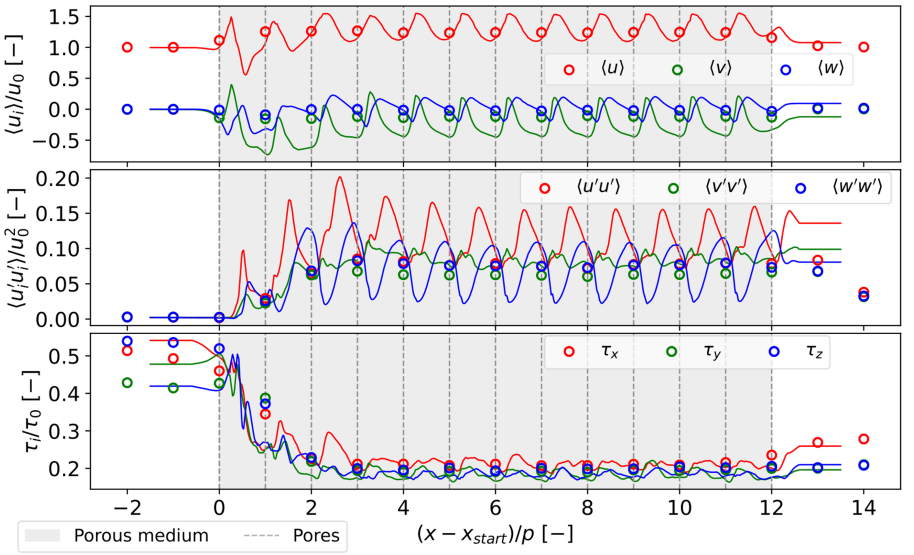


Figure 11. *Averaged mean fields along the longitudinal axis in the x_1-direction: velocity components $\langle u_i \rangle$, normal RST components $\langle u_i' u_i' \rangle$ and integral time scales $\tau_i = \int_0^{+\infty} \rho_{ii}(\vec{x_0}, t')\, dt'$, where $\rho_{ii}(\vec{x_0}, t')$ is the temporal autocorrelation function of the velocity component u_i at the spatial location $\vec{x_0}$ for a time shift t' (Pope, 2000, pp. 65–73). Empty circles ('o') represent full transversal section averages while lines ('—') are averages along the centre line of each pore.*

region often represents a critical zone where flame stabilisation depends on precise control of turbulence properties.

In the specific configuration considered here, defined by the pore scale, porosity and inlet flow conditions, the adaptation region spans approximately three pores. Beyond this region, turbulence is fully adapted to the pore scale, in agreement with the pore-scale prevalence hypothesis (Uth et al., 2016), which posits that, in a porous medium, the size of turbulent structures is constrained by the pore scale. In this fully adapted region, the flow can be considered statistically developed. At the outlet, as the flow exits the porous matrix, the eddies begin to merge once more, in a manner reminiscent of decaying grid-generated turbulence.

An illustrative example of physical outcomes that can be extracted from this simulation is given in Figure 11. However, results analysis and further physical discussions are beyond the scope of this paper.

5. Conclusions

A numerical approach has been developed to study turbulent flows through complex porous media, achieving a good compromise between accuracy and computational cost. The method relies on an SD solver, the JAGUAR code (ONERA–CERFACS ©), combining IBCs with the PGS approach to efficiently tackle complex geometries in low-Mach-number conditions. The approach has been validated using an SD polynomial order $p = 4$ through a series of three benchmark tests on simplified porous configurations.

First, for IBC validation, SD simulations using IBCs were compared with those based on classical body-fitted meshes. The main challenge with IBCs lies in accurately capturing near-wall phenomena such as BLs and stagnation or recirculation zones. Our results show that the average relative error in the L_2 norm for first- and second-order mean velocity fields remains below 1%, with local discrepancies, primarily near walls and in wake regions, limited to 5.5% in the L_∞ norm. These differences do not alter the overall mean flow behaviour, confirming that the IBC implementation faithfully reproduces the mean dynamics while significantly reducing meshing complexity around intricate geometries.

https://doi.org/10.1017/flo.2025.10036 Published online by Cambridge University Press

Second, for PGS validation, SD simulations with and without the PGS method were compared. The selected PGS factor increases the effective time step by a factor of $\alpha = 4.5$. While the PGS method introduces slight modifications to the pressure field under incompressibility assumptions and filters out high-frequency content, we observed good agreement in both mean flow statistics and energy spectra. The average L_2 norm errors for first- and second-order velocity moments are below 4.5% and 3.5%, respectively. The energy spectra correctly capture the relevant peaks and magnitudes of dominant frequencies, with very limited relative errors, mainly concentrated in the wake downstream of the porous section. These results confirm that the PGS method preserves the essential flow physics while significantly accelerating simulations.

Third, for the porous medium reference case, the SD-DNS approach, employing both PGS and IBCs, was compared with the classical porous medium simulation by Jin et al. (2015) using FVM-DNS. The SD solver reproduces the normalised turbulent two-point correlations R_{ii}/u_m^2 with high accuracy. A slight underestimation of the peak values is observed, attributed to reduced near-wall dissipation introduced by the IBCs, which leads to marginally lower fluctuation levels.

Finally, we applied the developed approach to a complex porous geometry involving approximately a quarter of a billion degrees of freedom. The configuration consists of a TPMS porous medium of Gyroid type, with porosity $\varphi = 0.90$, traversed by an injected turbulent flow at an inlet Reynolds number of $Re = 2500$, turbulence intensity of $\mathrm{Tu} = 10\%$, and energy-containing turbulent scales twice the pore cell size. This case introduces the novel consideration of injected turbulence as a boundary condition, representative of realistic engineering applications.

Overall, this work presents an alternative high-fidelity numerical strategy to traditional FVM-DNS and LBM-DNS approaches for the study of complex porous flows. In future work, we aim to apply this methodology to TPMS porous media to investigate how pore shape, porosity and injection parameters influence the interaction between turbulence and porous structures.

Supplementary material. Animations illustrating the application case, described in Section 4, are available online at the following link: https://www.youtube.com/@porous\media\channel. The supplementary material for this article can be found at https://doi.org/10.1017/flo.2025.10036.

Data and coding availability statement. Raw data and post-treatment codes are available from the corresponding author.

Author contributions. Adrian Rusnak: Investigation, Formal analysis, Data curation, Visualisation, Writing – Original draft. François Chedevergne: Conceptualisation, Methodology, Supervision, Writing – Review & Editing. Rémi Roncen: Conceptualisation, Methodology, Supervision, Project administration, Funding acquisition, Writing – Review & Editing.

Funding statement. The authors thank H. Deniau, T. Marchal, E. D'Ayer and A. Colombié for their support with the JAGUAR simulations and post-processing. Co-funded by the European Union (ERC, POROLEAF, 101103502). Views and opinions expressed are, however, those of the authors only and do not necessarily reflect those of the European Union or the European Research Council Executive Agency. Computational resources were provided by GENCI at TGCC under the grants 2024-SS012A15391 and 2025-A0172B15655 on the supercomputer IRENE's SKL Partition.

Declaration of generative AI and AI-assisted technologies in the writing process. During the writing of the original draft, A. Rusnak used ChatGPT in order to improve language and readability. After using this tool, the authors reviewed and edited the content as needed and take full responsibility for the content of the publication.

Declaration of interests. The authors declare no conflict of interest.

Appendix A. The IBC impact: near-wall flow and pressure drop

Using IBCs naturally introduces near-wall errors, which are intrinsic to the artificial modelling. In Section 3.1, we showed that IBC results closely match classical body-fitted simulations for both first-

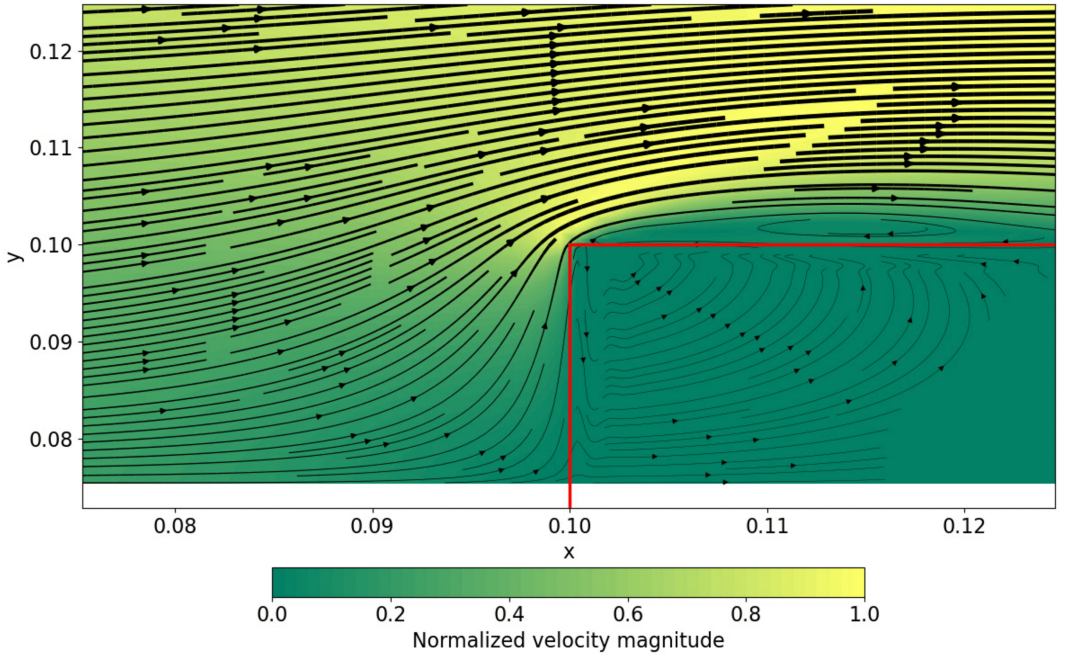


Figure A1. *The IBC validation (case with IBCs): streamlines around the upstream corner of the solid. Red lines indicate the exact solid edges.*

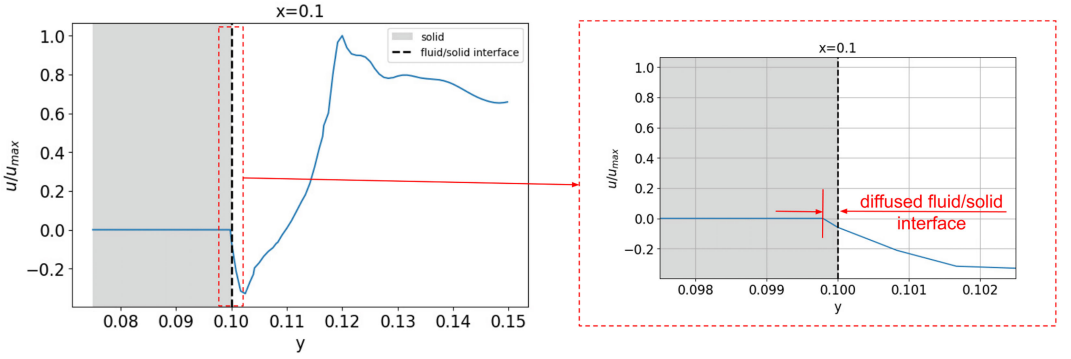


Figure A2. *The IBC validation (case with IBCs): cross-wise profile of the streamwise velocity at the solid edge (x = 1 in Figure A1). The diffused interface layer due to the continuous IBC is highlighted.*

and second-order velocity statistics. Here, we focus on the near-wall region to illustrate the diffused fluid–solid interface and the influence of VP on the pressure gradient.

Figure A1 shows the velocity streamlines at the edge $(x, y) = (0.1, 0.1)$ of the solid bar. The corresponding streamwise velocity profile along $x = 1$ is shown in Figure A2. A thin diffused layer of size $h/d \sim 10^{-3}$, characteristic of continuous IBM approaches, appears with normalised BL velocities of 10^{-5}–10^{-7}, while the velocity inside the solid remains effectively zero. The sharp solid edge is preserved, although a slight curvature proportional to h/d smooths the boundary locally.

Figure A3 reports the pressure drop $\Delta p = p_{\text{out}} - p_{\text{in}}$ measured by probes upstream and downstream of the obstacle. The relative difference between IBC and body-fitted cases is approximately $+0.45\%$

https://doi.org/10.1017/flo.2025.10036 Published online by Cambridge University Press

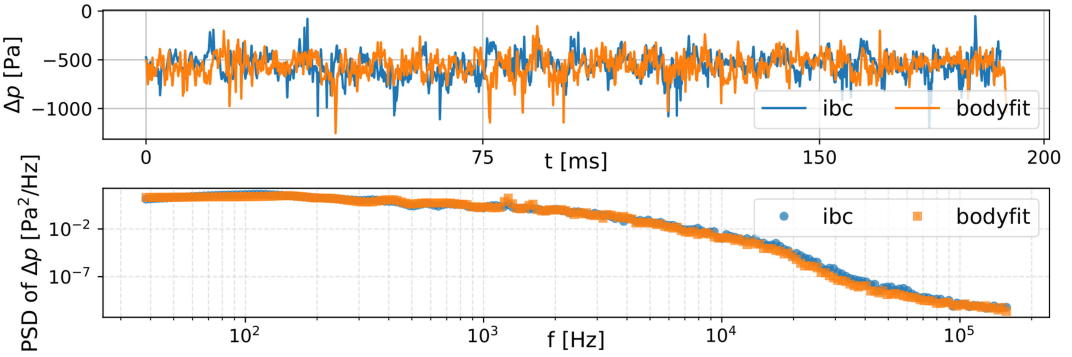


Figure A3. *The IBC validation: pressure drop measured between upstream and downstream probes (top) and corresponding frequency spectrum (bottom).*

for the mean and 9.0% for the variance (Figure A3, top). The corresponding pressure-drop spectrum (Figure A3, bottom) shows only marginal spectral discrepancies.

Appendix B. The PGS impact: pressure drop

The main requirement of the PGS method is the low-inhomogeneity assumption. In our study, pressure variations remained well within this condition ($p'/\bar{p} \ll 1\%$) across most of the domain. Slight deviations up to 2% were observed near the walls due to the IBCs, but these are very localised and negligible in magnitude. Moreover, the averaged pressure drop in the streamwise direction was almost unchanged after introducing the PGS, as illustrated in Figure B1.

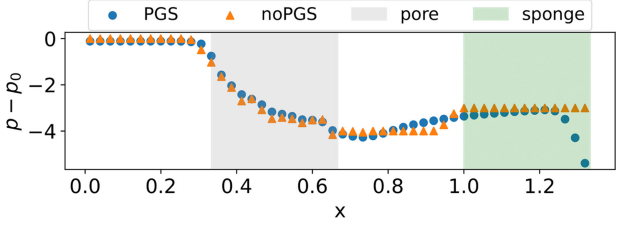


Figure B1. *The PGS validation: averaged pressure drop ($p - p_0$) along the streamwise direction x, where p_0 is the inlet pressure.*

Appendix C. Von Kármán-Pao (VKP) spectrum definition

The VKP energy spectrum $E(\kappa)$ in wavenumber space κ as defined by Pao (1965) as $E(\kappa) = \beta u_{rms}'^2/\kappa_e\,(\kappa/\kappa_e)^4\,(1+(\kappa/\kappa_e)^2)^{-17/6}\exp(-2\,(\kappa/\kappa_{\mathrm{Kol}})^2)$, where β is a scaling coefficient, κ_e corresponds to the VKP spectrum energy-containing wavenumber and κ_{Kol} denotes the Kolmogorov wavenumber. Assuming HIT in the limit of infinite Reynolds number, meaning $(\kappa_{\mathrm{Kol}}/\kappa_e)^2 \to \infty$, the integral of the spectrum can be enforced to match the turbulent kinetic energy as $\int E(\kappa)\,d\kappa = \mathrm{TKE} = 3/2u_{rms}'^2$ which leads to the approximate value $\beta \approx 1.45$. Note that the maximum of the VKP spectrum occurs at the wavenumber $\kappa_{e_{max}} = \sqrt{12/5}\,\kappa_e$. Thus the other parameters of the isotropic VKP spectrum are given by $L_e = \sqrt{12/5}\pi/(2u_{rms}'^2)\int E(\kappa)/\kappa\,d\kappa$ and $\kappa_{\mathrm{Kol}} = \left(\epsilon/\nu^3\right)^{1/4} = \left[(2\nu\int \kappa^2 E(\kappa)\,d\kappa)/\nu^3\right]^{1/4}$. Therefore, the spectrum can be fully characterised by u'_{rms} and κ_e. However, in practical applications, where the Reynolds number is finite (albeit large), the VKP spectrum limits $[\kappa_e, \kappa_{\mathrm{Kol}}]$ have to be explicitly defined as HIT assumptions are no longer valid. The strategy adopted in this case

https://doi.org/10.1017/flo.2025.10036 Published online by Cambridge University Press

consists in constructing a spectrum that approximates as closely as possible the one under HIT conditions. We prescribe the energy-containing eddy length scale $L_{e,\mathrm{VKP}}$, the Kolmogorov length scale κ_{Kol} and the turbulent intensity rate $Tu = u'_{rms}/u_0$, such that a target root-mean-square turbulence intensity $u'_{rms} = \mathrm{Tu} \cdot u_0$ at the inlet Reynolds number $Re = u_0 L/\nu$ is achieved. The amplitude β of the spectrum is then obtained by solving an optimisation problem of the type $\min_\beta\ (\epsilon_L + \epsilon_k)$ aimed at minimising the relative errors on the TKE $\epsilon_k = \left| \int E(\kappa)\, d\kappa - 3/2 u'^2_{rms} \right| / u'^2_{rms}$ and the integral length scale $\epsilon_L = \left| L_{e_{\max}} - \pi/(2u'^2_{rms}) \int E(\kappa)/\kappa\, d\kappa \right| / L_{e_{\max}}$ if compared with the HIT solutions.

References

Arquis, E., & Caltagirone, J. P. (1984). On the hydrodynamical boundary conditions along a fluid layer porous medium interface: Application to the case of free-convection. *Comptes Rendus De l'Academie Des Sciences (Serie II)*, *299*(1), 1–4.

Boigné, E., Muhunthan, P., Mohaddes, D., Wang, Q., Sobhani, S., Hinshaw, W., & Ihme, M. (2019). X-ray computed tomography for flame-structure analysis of laminar premixed flames. *Combustion and Flame*, *200*, 142–154.

Cassagne, A., Boussuge, J.-F., Villedieu, N., Puigt, G., D'Ast, I., & Genot, A. (2015). JAGUAR: a new CFD code dedicated to massively parallel high-order LES computations on complex geometry. In Proceedings of the 50th 3AF international conference on applied aerodynamics.

Chu, X., Weigand, B., & Vaikuntanathan, V. (2018). Flow turbulence topology in regular porous media: from macroscopic to microscopic scale with direct numerical simulation. *Physics of Fluids*, *30*(6).

D'Ayer, H., Colombié, A., Dounia, O., & Chedevergne, F. (2025). Immersed boundary conditions using the spectral difference method applied to turbulent flows over rough surfaces. *Under Consideration in Computers and Fluids Journal*, HAL archive: hal-05075852.

De Lemos, M. J. S. (2005). *Transport phenomena in porous media* (vol. *III*, pp. 1–33). Elsevier.

De Lemos, M. J. S. (2012). *Turbulence in porous media* (2nd edn.). Elsevier.

Diao, Z., Chen, Z., Liu, H., Wei, B., & Hou, J. (2023). Pore-scale modeling of gravity-driven superheated vapor flooding process in porous media using the lattice Boltzmann method. *International Communications in Heat and Mass Transfer*, *146*, 106937.

Fattahi, E., Waluga, C., Wohlmuth, B., Rüde, U., Manhart, M., & Helmig, R. (2016). Lattice boltzmann methods in porous media simulations: From laminar to turbulent flow. *Computers & Fluids*, *140*, 247–259.

Gasow, S., Kuznetsov, A. V., Avila, M., & Jin, Y. (2021). A macroscopic two-length-scale model for natural convection in porous media driven by a species-concentration gradient. *Journal of Fluid Mechanics*, *926*, A8.

Gasow, S., Lin, Z., Zhang, H. C., Kuznetsov, A. V., Avila, M., & Jin, Y. (2020). Effects of pore scale on the macroscopic properties of natural convection in porous media. *Journal of Fluid Mechanics*, *891*, A25.

Gasow, S., Lin, Z., Zhang, H. C., Kuznetsov, A. V., Avila, M., & Jin, Y. (2022). Prediction of pore-scale-property dependent natural convection in porous media at high Rayleigh numbers. *International Journal of Thermal Sciences*, *179*, 107635.

He, X., Apte, S., Schneider, K., & Kadoch, B. (2018). Angular multiscale statistics of turbulence in a porous bed. *Physical Review Fluids*, *3*(8), 084501.

He, X., Apte, S. V., Finn, J. R., & Wood, B. D. (2019). Characteristics of turbulence in a face-centred cubic porous unit cell. *Journal of Fluid Mechanics*, *873*.

Jin, Y., & Kuznetsov, A. V. (2017). Turbulence modeling for flows in wall bounded porous media: An analysis based on direct numerical simulations. *Physics of Fluids*, *29*(4).

Jin, Y., & Kuznetsov, A. V. (2024). Multiscale modeling and simulation of turbulent flows in porous media. *International Journal of Fluid Engineering*, *1*(1).

Jin, Y., Uth, M. F., Kuznetsov, A. V., & Herwig, H. (2015). Numerical investigation of the possibility of macroscopic turbulence in porous media: A direct numerical simulation study. *Journal of Fluid Mechanics*, *766*, 76–103.

Kazerooni, R. B., & Hannani, S. K. (2007). Simulation of turbulent flow through porous media employing a v2f model. *AIP Conference Proceedings*, *963*, 1257–1260.

Kolomenskiy, D., & Schneider, K. (2009). A fourier spectral method for the Navier–Stokes equations with volume penalization for moving solid obstacles. *Journal of Computational Physics*, *228*(16), 5687–5709.

Kopriva, D. A. (1998). A staggered-grid multidomain spectral method for the compressible Navier–Stokes equations. *Journal of Computational Physics*, *143*, 125–158.

Kuwahara, F., Kameyama, Y., Yamashita, S., & Nakayama, A. (1998). Numerical modeling of turbulent flow in porous media using a spatially periodic array. *Journal of Porous Media*, *1*, 47–55.

Kuwahara, F., Yamane, T., & Nakayama, A. (2006). Large eddy simulation of turbulent flow in porous media. *International Communications in Heat and Mass Transfer*, *33*(4), 411–418.

Liu, Q., & Vasilyev, O. V. (2007). A Brinkman penalization method for compressible flows in complex geometries. *Journal of Computational Physics*, *227*(2), 946–966.

Liu, H., Sun, S., Wu, R., Wei, B., & Hou, J. (2021). Pore-scale modeling of spontaneous imbibition in porous media using the lattice Boltzmann method. *Water Resources Research*, *57*(6), e2020WR029219.

https://doi.org/10.1017/flo.2025.10036 Published online by Cambridge University Press

Liu, W., Shi, L., & Liu, H. (2023). Numerical study of the impact of geometrical parameters on the rarefied gas transport in porous media. *Gas Science and Engineering*, *110*, 204855.

Lucci, F., Della Torre, A., Montenegro, G., Kaufmann, R., & Eggenschwiler, P. D. (2017). Comparison of geometrical, momentum and mass transfer characteristics of real foams to Kelvin cell lattices for catalyst applications. *International Journal of Heat and Mass Transfer*, *108*, 341–350.

Ma, X., & Su, Z. (2020). Development of acoustic liner in aero engine: A review. *Science China Technological Sciences*, *63*, 2491–2504.

MacNamara, S., & Strang, G. (2016). *Splitting methods in communication, imaging, science, and engineering* (pp. 95–114). Springer International Publishing.

Marchal, T., Deniau, H., Boussuge, J. F., Cuenot, B., & Mercier, R. (2023). Extension of the spectral difference method to premixed laminar and turbulent combustion. *Flow, Turbulence and Combustion*, *111*, 141–176.

Masuoka, T., & Takatsu, Y. (1996). Turbulence model for flow through porous media. *International Journal of Heat and Mass Transfer*, *39*, 2803–2809.

Mittal, R., & Iaccarino, G. (2005). Immersed boundary methods. *Annual Review of Fluid Mechanics*, *37*, 239–261.

Nakayama, A., & Kuwahara, F. (2008). A general macroscopic turbulence model for flows in packed beds, channels, pipes, and rod bundles. *Journal of Fluids Engineering*, *130*(10).

Pao, Y.-H. (1965). Structure of turbulent velocity and scalar fields at large wavenumbers. *Physics of Fluids*, *8*(6), 1063–1075.

Papageorgakis, G. C., & Assanis, D. N. (1999). Comparison of linear and nonlinear RNG-based k-epsilon models for incompressible turbulent flows. *Numerical Heat Transfer, Part B: Fundamentals*, *35*(1), 1–22.

Pedras, M. H. J., & De Lemos, M. J. S. (2003). Computation of turbulent flow in porous media using a low Reynolds number k-ϵ model and an infinite array of transversely displaced elliptic rods. *Numerical Heat Transfer, Part A*, *43*, 585–602.

Pope, S. B. (2000). *Turbulent flows*. Cambridge University Press.

Ramshaw, J. D., O'Rourke, P. J., & Stein, L. R. (1985). Pressure gradient scaling method for fluid flow with nearly uniform pressure. *Journal of Computational Physics*, *58*(3), 361–376.

Rao, F., & Jin, Y. (2022). Possibility for survival of macroscopic turbulence in porous media with high porosity. *Journal of Fluid Mechanics*, *937*, A17.

Rashidi, S., Kashefi, M. H., Kim, K. C., & Samimi-Abianeh, O. (2019). Potentials of porous materials for energy management in heat exchangers. *Applied Energy*, *243*, 206–232.

Spiteri, R. J., & Ruuth, S. J. (2002). A new class of optimal high-order strong-stability-preserving time discretization methods. *SIAM Journal on Numerical Analysis*, *40*(2), 469–491.

Srikanth, V., Huang, C.-W., Su, T. S., & Kuznetsov, A. V. (2021). Symmetry breaking of turbulent flow in porous media composed of periodically arranged solid obstacles. *Journal of Fluid Mechanics*, *929*(A2).

Suga, K. (2016). Understanding and modeling turbulence over and inside porous media. *Flow, Turbulence and Combustion*, *96*(3), 717–756.

Teruna, C., Manegar, F., Avallone, F., Ragni, D., Casalino, D., & Carolus, T. (2020). Noise reduction mechanisms of an open-cell metal-foam trailing edge. *Journal of Fluid Mechanics*, *898*, A18.

Toro, E. (2009). *Riemann solvers and numerical methods for fluid dynamics: A practical introduction* (3rd edn.). Springer.

Trimis, D., & Durst, F. (1996). Combustion in a porous medium: Advances and applications. *Combustion Science and Technology*, *121*(1-6), 153–168.

Uth, M.-F., Jin, Y., Kuznetsov, A. V., & Herwig, H. (2016). A direct numerical simulation study on the possibility of macroscopic turbulence in porous media: effects of different solid matrix geometries, solid boundaries, and two porosity scales. *Physics of Fluids*, *28*(6).

Vanharen, J., Puigt, G., Vasseur, X., Boussuge, J.-F., & Sagaut, P. (2017). Revisiting the spectral analysis for high-order spectral discontinuous methods. *Journal of Computational Physics*, *337*, 379–402.

Veilleux, A., Puigt, G., Deniau, H., & Daviller, G. (2022). A stable spectral difference approach for computations with triangular and hybrid grids up to the 6th order of accuracy. *Journal of Computational Physics*, *449*, 110774.

Wang, J., Chen, K., Zeng, M., Ma, T., Wang, Q., & Cheng, Z. (2023). Investigation on flow and heat transfer in various channels based on triply periodic minimal surfaces (TPMS). *Energy Conversion and Management*, *283*, 116955.

Wang, W., Chu, X., Lozano-Durán, A., Helmig, R., & Weigand, B. (2021). Information transfer between turbulent boundary layers and porous media. *Journal of Fluid Mechanics*, *920*, A21.

Wang, W., Lozano-Durán, A., Helmig, R., & Chu, X. (2022). Spatial and spectral characteristics of information flux between turbulent boundary layers and porous media. *Journal of Fluid Mechanics*, *949*, A16.

Wood, B. D., He, X., & Apte, S. V. (2020). Modeling turbulent flows in porous media. *Annual Review of Fluid Mechanics*, *52*(1), 171–203.

Wood, S., & Harris, A. T. (2008). Porous burners for lean-burn applications. *Progress in Energy and Combustion Science*, *34*(5), 667–684.

Cite this article: Rusnak A., Chedevergne F. and Roncen R. (2025). Direct numerical simulations of turbulent flows through porous media using a spectral difference method solver. *Flow*, *5*, E43. https://doi.org/10.1017/flo.2025.10036

https://doi.org/10.1017/flo.2025.10036 Published online by Cambridge University Press